PNAS RESEARCH ARTICLE | PHYSIOLOGY

Osteoblast-lineage calcium/calmodulin-dependent kinase 2 delta and gamma regulates bone mass and quality

Jenna M. Leser[a], Olivia M. Torre[a], Nicole R. Gould[a], Qiaoyue Guo[a], Heather V. Buck[a], Joe Kodama[a], Satoru Otsuru[a], and Joseph P. Stains[a,1]

Edited by Clifford Tabin, Harvard Medical School, Boston, MA; received March 17, 2023; accepted September 30, 2023

Bone regulates its mass and quality in response to diverse mechanical, hormonal, and local signals. The bone anabolic or catabolic responses to these signals are often received by osteocytes, which then coordinate the activity of osteoblasts and osteoclasts on bone surfaces. We previously established that calcium/calmodulin-dependent kinase 2 (CaMKII) is required for osteocytes to respond to some bone anabolic cues in vitro. However, a role for CaMKII in bone physiology in vivo is largely undescribed. Here, we show that conditional codeletion of the most abundant isoforms of CaMKII (delta and gamma) in mature osteoblasts and osteocytes [Ocn-cre:*Camk2d*/*Camk2g* double-knockout (dCKO)] caused severe osteopenia in both cortical and trabecular compartments by 8 wk of age. In addition to having less bone mass, dCKO bones are of worse quality, with significant deficits in mechanical properties, and a propensity to fracture. This striking skeletal phenotype is multifactorial, including diminished osteoblast activity, increased osteoclast activity, and altered phosphate homeostasis both systemically and locally. These dCKO mice exhibited decreased circulating phosphate (hypophosphatemia) and increased expression of the phosphate-regulating hormone fibroblast growth factor 23. Additionally, dCKO mice expressed less bone-derived tissue nonspecific alkaline phosphatase protein than control mice. Consistent with altered phosphate homeostasis, we observed that dCKO bones were hypo-mineralized with prominent osteoid seams, analogous to the phenotypes of mice with hypophosphatemia. Altogether, these data reveal a fundamental role for osteocyte CaMKIIδ and CaMKIIγ in the maintenance of bone mass and bone quality and link osteoblast/osteocyte CaMKII to phosphate homeostasis.

osteoblast | osteocyte | CaMKII | bone | phosphate

Significance

Genetic deletion of CaMKIIδ/CaMKIIγ in late osteoblasts and osteocytes severely impairs post-natal bone mass acquisition and bone quality, resulting in severe osteopenia and skeletal fragility. The phenotype is multifactorial with reduced osteoblast number and activity, increased osteoclast number and activity, diminished bone-derived and circulating FGF23 (fibroblast growth factor 23), resultant hypophosphatemia, and decreased bone-derived alkaline phosphatase. The altered phosphate homeostasis results in mineralization defects comparable to mice overexpressing FGF23 or devoid of TNAP (tissue nonspecific alkaline phosphatase). These data reveal a fundamental role for CaMKIIδ /CaMKIIγ in bone physiology.

Bone undergoes a dynamic process of bone formation and resorption to maintain bone mass and quality, while also regulating systemic calcium and phosphate homeostasis. Often, bone-embedded osteocytes sense and respond to a complex milieu of mechanical, hormonal, and local signals and then direct osteoblasts and osteoclasts to mount an anabolic or catabolic response to these signals (1–5). When osteoclast activity exceeds osteoblast activity, bone mass is reduced and, if sustained, can result in skeletal fragility and a propensity for fractures. Conversely, factors resulting in activation of osteoblasts and a net increase in bone anabolism can improve bone mass and reduce fracture risk. Accordingly, understanding factors and pathways that can be targeted to regulate bone acquisition or destruction is important.

Our group previously established a role for calcium/calmodulin-dependent kinase 2 (CaMKII) in osteocytes and the posttranslational control of sclerostin (6–8). Sclerostin is an important and therapeutically relevant repressor of osteoblastogenesis and bone formation (9). Specifically, our initial finding revealed that mechanical loading–induced production of reactive oxygen species from NOX2, influx of calcium into the osteocyte, and activation of CaMKII were obligated for the rapid, minutes timescale, loss of sclerostin protein (6). Subsequently, we found that the posttranslational loss of sclerostin protein was a result of rapid lysosomal degradation. Using a combination of in vitro, in vivo, and ex vivo models, we showed this lysosomal degradation of sclerostin protein occurred in response to disparate bone anabolic stimuli, including mechanical loading and administration of parathyroid hormone (1 to 34) (PTH) (7). While the kinetics of the sclerostin degradation varied between loading and PTH, the obligated activation of CaMKII prior to the minutes timescale degradation of sclerostin (6–8) protein was common.

Calcium/calmodulin-dependent kinases are a family of serine/threonine kinases that contain a calmodulin-binding domain and are responsive to increases in intracellular calcium. CaMKII isoforms are encoded for by four genes: alpha, beta, delta, and gamma, each of which has a unique tissue and cell-type-specific expression profile (10). All CaMKII isoforms can be activated by binding of calcium and calmodulin, which allows CaMKII to tune its activity

Author affiliations: [a]Department of Othopaedics, University of Maryland School of Medicine, Baltimore, MD 21201

Author contributions: J.M.L., O.M.T., N.R.G., and J.P.S. designed research; J.M.L., O.M.T., N.R.G., Q.G., and H.V.B. performed research; J.K. and S.O. contributed new reagents/analytic tools; J.M.L., O.M.T., N.R.G., and J.P.S. analyzed data; H.V.B., J.K., and S.O. scientific input; and J.M.L. and J.P.S. wrote the paper.

The authors declare no competing interest.

This article is a PNAS Direct Submission.

[1]To whom correspondence may be addressed. Email: jstains@som.umaryland.edu.

This article contains supporting information online at https://www.pnas.org/lookup/suppl/doi:10.1073/pnas.2304492120/-/DCSupplemental.

Published November 17, 2023.

proportionally to the calcium and calmodulin responses (11). This calcium calmodulin response of CaMKII canonically leads to the autophosphorylation of Threonine 286, blocking autoinhibition and sustaining CaMKII activity. Active CaMKII regulates transcription factors and regulators of chromatin remodeling, establishing a role in transcriptional programming, as well as players involved in protein secretion, trafficking, and degradation, confirming a role as a determinant of post-translational protein fate (12–14).

While a lot is known about the function of CaMKII in the brain and the heart (15, 16), little is known about the role of CaMKII in bone in vivo. Some in vitro data suggested a possible role for CaMKII in regulating osteoblast differentiation (17, 18). Given our data showing that CaMKII is an integrator of some bone anabolic cues by osteocytes, we wanted to confirm a role of osteoblast/osteocyte CaMKII in bone homeostasis. Thus, we examined the simultaneous conditional deletion of the two isoforms of CaMKII expressed in bone, *Camk2d* and *Camk2g,* using Ocn-Cre and reveal an important role for CaMKIIδ and CaMKIIγ in the postnatal accrual of bone mass, maintenance of bone quality, and regulation of phosphate homeostasis.

Results

Conditional Deletion of *Camk2d* and *Camk2g* in Mature Osteoblasts and Osteocytes Using Osteocalcin-Cre. Previous work from our group demonstrated an important role for CaMKII in osteocyte response to some bone anabolic stimuli (6, 7, 19). In these experiments, we showed that signaling through CaMKII could initiate lysosomal degradation of sclerostin in response to mechanical loading and PTH. However, those studies used either the CaMKII inhibitor KN-93 or dominant negative CaMKIIα T286A, which do not discriminate CaMKII isoforms (20, 21). In order to use genetic models to investigate the role of CaMKII in osteocyte physiology, we first determined which isoforms are expressed in osteocytes. Primary osteocyte cultures and Ocy454 cells, an osteocyte-like cell line isolated from the Immortomouse (22), expressed both *Camk2d* and *Camk2g* but did not have detectable levels of either *Camk2a* or *Camk2b* (*SI Appendix*, Fig. S1 *A* and *B*). In whole cortical bone RNA extracts from flushed femurs, all four *Camk2* isoforms were detected (*SI Appendix*, Fig. S1*C*), likely due to the contribution from other cell types present including not only osteoblasts, osteoclasts, osteocytes, and their progenitors but also bone lining cells, vascular cells, neurons, residual bone marrow cells, and adipocytes.

CaMKIIδ and CaMKIIγ are often found coexpressed in mesenchymal tissues like skeletal muscle and their codeletion is often required to prevent compensation (23). Accordingly, we conditionally codeleted both *Camk2d* and *Camk2g* in mature osteoblasts and osteocytes by crossing *Camk2d* and *Camk2g* double-floxed mice (23) with osteocalcin-cre (Ocn-cre) mice (24) (*Camk2d/g* dCKO). Representative genotyping gel electrophoresis of Ocn-cre deleted *Camk2d/g* dCKO and *Camk2d/g*$^{fl/fl}$ littermates (Control) show the presence of floxed *Camk2d/g* alleles and cre transgene from tail snip samples (*SI Appendix*, Fig. S1*D*). Given CaMKII isoforms are present in other bone-resident cell types, we performed immunohistochemistry to confirm the deletion of CaMKII in osteocytes. Notably, antibodies to CaMKII are not isoform specific, and therefore, we are unable to distinguish isoforms. As expected, CaMKII is detected in osteocytes in control but not *Camk2d/g* dCKO mice, while expression of CaMKII remains detectable in the other cells types, in both control and *Camk2d/g* dCKO samples, including periosteal, vascular, and marrow areas where the Ocn-Cre is not expressed (*SI Appendix*, Fig. S1*E*).

Ocn-Cre:*Camk2d/Camk2g* Double Knockout Mice Develop Severe Osteopenia in the Axial and Appendicular Skeleton. Examination of the mice with dual x-ray absorptiometry (DXA) revealed a significant reduction in both bone mineral density and bone mineral content without any change in percentage fat mass and percent lean mass in 8-wk-old male and female *Camk2d/g* dCKO mice relative to control mice (Fig. 1 *A–D*). Importantly, this change in bone mass occurred despite no difference in body weight and body length (Fig. 1 *E* and *F*), as well as organ weight (*SI Appendix*, Fig. S1 *F–H*), between genotypes at this age. Throughout the manuscript, data are presented with male (white) and female (gray) mice combined because analysis of the sexes individually did not reveal any sexual dimorphism of this dCKO phenotype.

Next, we examined the bone microarchitecture in the femurs of 8-wk-old and 3-wk-old mice by microcomputed tomography (μCT), which revealed a striking loss of trabecular and cortical bone in the *Camk2d/g* dCKO femur compared to age-matched control femurs of both male and female mice (Fig. 1 *G–K*). Quantification of the trabecular compartment of the distal femur of 8-wk-old mice revealed a 72% reduction in the bone volume fraction (BV/TV), with a decrease in trabecular number (Tb.N) and a corresponding increase in trabecular separation (Tb.Sp), while trabecular thickness (Tb.Th) was unaffected (Fig. 1 *L–O*). This large reduction in trabecular bone was also observed in the 3-wk-old *Camk2d/g* dCKO mice (*SI Appendix*, Fig. S2 *A–D*, *Q*, and *R*).

Quantification of the cortical compartment at the femoral mid-diaphysis revealed that cortical thickness (Ct.Th) is reduced by 24% in the 8-wk *Camk2d/g* dCKO femurs compared to control femurs (Fig. 1*P*). Likewise, total cortical bone area (Ct.Ar) was decreased ~25% in *Camk2d/g* dCKO bones with a reduction in both the periosteal and endocortical perimeters in the 8-wk mice (Fig. 1 *Q–S*). At 3 wk of age, cortical bone area was reduced by ~15%; however, changes in cortical perimeter were not yet apparent in *Camk2d/g* dCKO mice at this timepoint (*SI Appendix*, Fig. S2 *E–H*, *S*, and *T*). A slight increase in cortical porosity was also observed in the *Camk2d/g* dCKO mice at 8 wk, but not at 3 wk (Fig. 1*T* and *SI Appendix*, Fig. S2*I*). Lastly, the moments of inertia (pMMI, *I*max, and *I*min), which predict bone strength based on bone geometry, are all significantly decreased in the 8-wk *Camk2d/g* dCKO mice (Fig. 1 *U–W*), although only the *I*min is significantly decreased in the 3-wk *Camk2d/g* dCKO mice (*SI Appendix*, Fig. S2 *J–L*).

To determine whether this low bone mass phenotype was limited to long bones or represented a more generalized severe osteopenia, we examined trabecular bone mass in the axial skeleton, including the lumbar 6 (L6) vertebra and skull. As was observed in the femur, the trabecular BV/TV in the L6 vertebra is significantly reduced approximately 66% in the *Camk2d/g* dCKO, at both 8 wk and 3 wk of age (Fig. 2 *A–E* and *SI Appendix*, Fig. S2*M*). Additionally, the L6 vertebra of 8-wk- and 3-wk-old mice have significantly thinner trabeculae (Tb.Th), decreased trabecular number and an increase in trabecular separation in *Camk2d/g* dCKO L6 vertebra (Fig. 2 *F–H* and *SI Appendix*, Fig. S2 *N–P*, *U*, and *V*). Likewise, there is a marked reduction in bone mass in the skull. Quantification of the occipital/supra-occipital bones revealed a reduced bone volume in the dCKO mice compared to the control mice at 8 wk of age (Fig. 2 *I* and *J*). In aggregate, these data reveal severe osteopenia in both the appendicular and axial skeleton with a loss of trabecular bone mass apparent as early as 3 wk of age and a cortical bone phenotype revealed as the mice continue to grow, supporting an important role of *Camk2d* and *Camk2g* in bone mass acquisition.

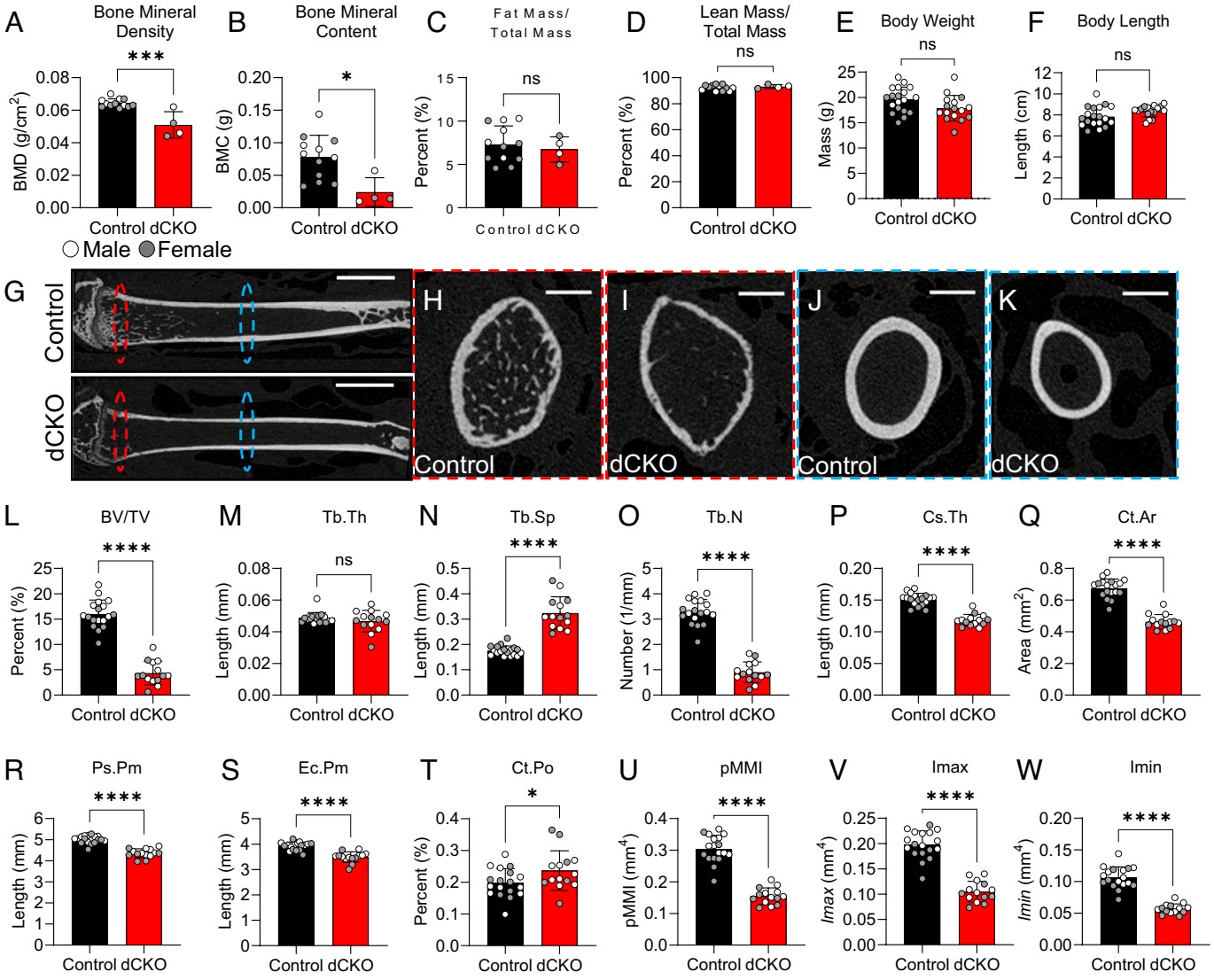

Fig. 1. Detection of low bone mass and altered microarchitecture in the appendicular skeleton of Ocn-cre:*Camk2d/Camk2g* dCKO mice. DXA measurements of 8-wk-old male (white) and female (gray) control and dCKO mice for (*A*) bone mineral density, (*B*) bone mineral content, (*C*) fat mass normalized to total mass, and (*D*) lean mass normalized to total mass (control n = 12, dCKO n = 4). Measurements of 8-wk-old control and dCKO mice for (*E*) body weight and (*F*) body length (control n = 19, dCKO n = 16). 2-D images from 8-wk-old μCT scanned femurs displaying (*G*) longitudinal cross-sections, the scale bar represents 2 mm, with representative ovals highlighting in red (*H* and *I*) longitudinal cross-sections of the trabecular compartment, the scale bar represents 500 μm (*J* and *K*) transverse cross-sections of the femoral midshaft and in blue, the scale bar represents 500 μm. Analyses of the trabecular compartment for male (white) and female (gray) (control n = 18, dCKO n = 14) (*L*) bone volume/tissue volume, (*M*) trabecular thickness, (*N*) trabecular spacing, and (*O*) trabecular number. Analyses of the cortex for male (white) and female (gray) (*P*) cross-sectional thickness, (*Q*) cortical bone area, (*R*) periosteal perimeter, (*S*) endocortical perimeter, (*T*) cortical porosity, (*U*) mean polar moment of inertia, (*V*) maximum moment of inertia, and (*W*) minimum moment of inertia. Graphs display the average ± SD with an unpaired *t* test analysis of the data.

While we did not see any differences in body weight and length at 8 wk of age, it is not uncommon to see growth deficits as a consequence of osteoblast-lineage-specific knockouts in mice (25, 26); therefore, we looked earlier. At 3 wk of age, there was no discrepancy between the weight and the length of the mice (*SI Appendix*, Fig. S3 *A* and *B*) nor were there any changes in femur length (*SI Appendix*, Fig. S3*C*). Additionally, we did not observe any overt defects in skeletal patterning by whole-body X-ray (*SI Appendix*, Fig. S3*D*). Given the expression of Ocn-cre at E18.5 (24), we assessed the presence of any developmental patterning defect in the dCKO mice with whole-mount staining of neonatal mice. No overt developmental defects were observed in our *Camk2d/g* dCKO mice at P1 (*SI Appendix*, Fig. S3*E*). Thus, deletion of *Camk2d* and *Camk2g* just prior to birth does not overtly contribute to skeletal development or patterning. Rather, the apparent osteopenia seems a result of a defect in postnatal bone mass acquisition.

dCKO Mice Have Reduced Periosteal Bone Formation and Increased Bone Resorption. To understand the cellular basis of the observed low bone mass in these *Camk2d/g* dCKO mice, we performed dynamic histomorphometry in 8-wk-old male mice (Fig. 3 *A*–*C* and *SI Appendix*, Fig. S4 *A*–*C*). On the periosteal surface of cortical bone, osteoblast activity was reduced *Camk2d/g* dCKO mice compared to control mice. Both the periosteal mineralizing surface/bone surface (Ps.MS/BS), which represents the fraction of the bone surface in which osteoblasts are active, and the periosteal bone formation rate (Ps.BFR), which represent the work done by each osteoblast multiplied by the percentage of bone, were significantly decreased in the *Camk2d/g* dCKO

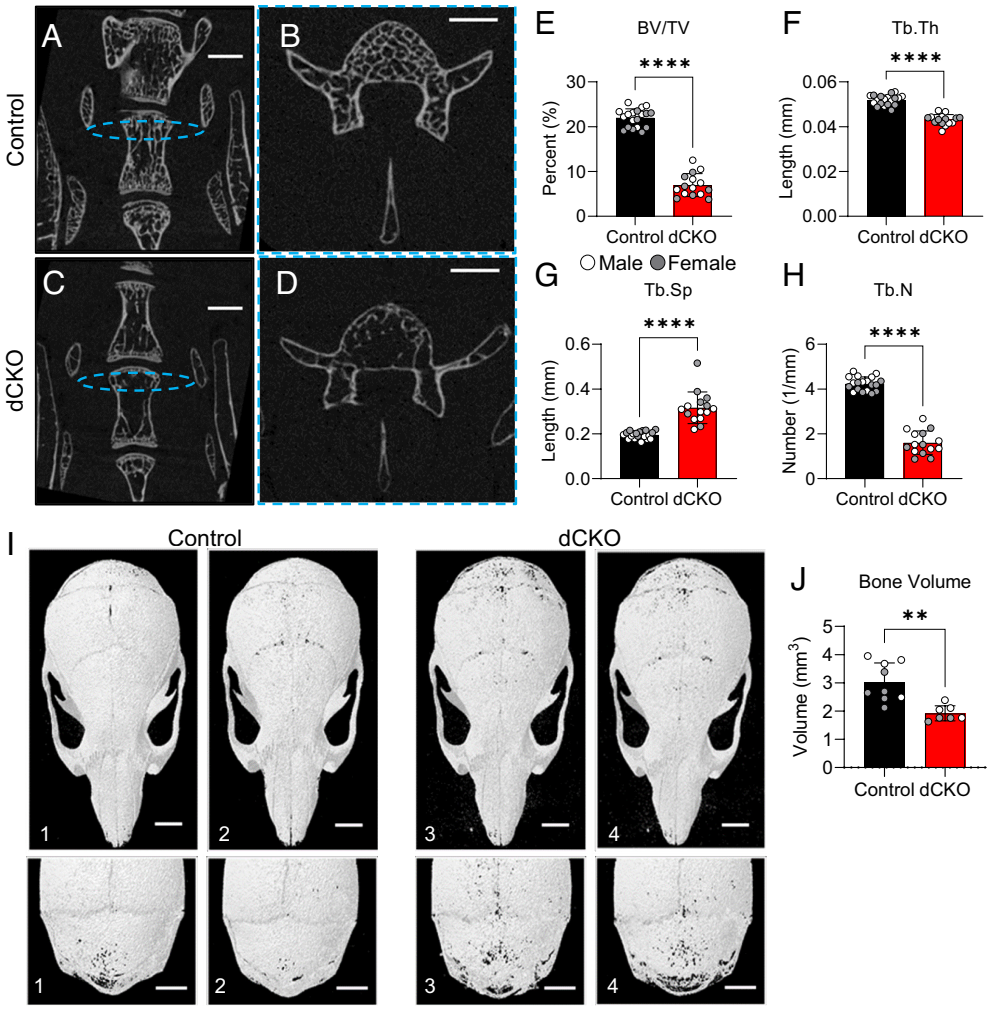

Fig. 2. Detection of osteopenia and altered microarchitecture in the axial skeleton of Ocn-cre:*Camk2d/Camk2g* dCKO mice. 2-D images from 8-wk-old μCT scanned L6 vertebra displaying longitudinal cross-sections (scale bar represents 1mm) and transverse cross-sections (scale bar represents 500μm), respectively, in control (*A* and *B*) and dCKO (*C* and *D*) mice. The blue ovals in the longitudinal sections indicate the location of the transverse image. Analyses of the L6 vertebra trabecular compartment for male (white) and female (gray) (control n = 19, dCKO n = 15) showing (*E*) bone volume/tissue volume, (*F*) trabecular thickness, (*G*) trabecular spacing, and (*H*) trabecular number. (*I*) Representative 3D reconstructions of control (panels 1 and 2) and dCKO (panels 3 and 4) skulls, the scale bars represent 2 mm, with (*J*) quantification of the occipital/supra-occipital bone volume (control n = 9, dCKO n = 7). Graphs display the average ± SD with an unpaired *t* test analysis of the data.

mice (Fig. 3 *A* and *C*). The periosteal mineral apposition rate (Ps.MAR), which represents the work done by each osteoblast, was also reduced but did not reach statistical significance (Fig. 3*B*). Together, these data suggest that there is a defect in the number of active osteoblasts on the periosteal surface likely reducing cortical modeling and contributing to the reduced periosteal perimeter. In contrast, endocortical (Ec.) measures of bone formation, including MS/BS, BFR, and MAR were unaffected by the deletion of *Camk2g* and *Camk2g* by Ocn-cre (*SI Appendix*, Fig. S4 *A–C*). Consistent with these measures of dynamic histomorphometry, using RNAscope for *Col1a1* in longitudinal sections of the femur (*SI Appendix*, Fig. S4 *D–I*), we saw a decrease in the periosteal osteoblast surface/bone surface in the dCKO mice, although it did not reach statistical significance (*SI Appendix*, Fig. S4*D*). On the endocortical surface, we observed no change in osteoblast surface/bone surface (*SI Appendix*, Fig. 4*E*). We also noted a slight decrease in the trabecular osteoblast surface/trabecular bone surface, yet this percentage of label surfaced was not statistically significant although substantially less trabecular bone was present in these dCKO mice (*SI Appendix*, Fig. S4*F*).

These distinct envelope (periosteal vs. endosteal)-specific effects on osteoblast activity and, to a lesser extent, osteoblast number suggest that factors regulating osteoblast function or mineralization may be important to the cortical bone phenotype in dCKO mice, rather than a cell-autonomous defect in the osteoblast lineage. Consistent with the notion that osteoblast themselves are functional but may be receiving different cues on distinct envelopes, RT-qPCR from whole bone RNA extracts revealed no impact of the double knockout on gene expression of osteoblast/osteocyte markers (Fig. 3*D*). Likewise, adenoviral-Cre-mediated deletion of the floxed *Camk2d/g* alleles in primary cells in vitro revealed no changes in osteoblast/osteocyte gene expression (*SI Appendix*, Fig. S4*J*). Surprisingly, serum P1NP, a marker of collagen synthesis and crude estimate of bone formation, reveals no major effect of *Camk2d* and *Camk2g* deletion (Fig. 3*E*) despite reduced bone formation rates and slightly reduced osteoblast number, perhaps due to the relative insensitivity of serum P1NP assays relative to dynamic histomorphometry.

With respect to bone resorption, osteoclast number and activity are elevated in dCKO mice, as the osteoclast surface/bone surface ratio in the trabecular compartment of the femurs (Fig. 3 *F* and *G*) and serum CTX (carboxy-terminal crosslinks), a marker of osteoclast activity, are increased (Fig. 3*H*) in the dCKO mice at 8 wk of age. Since the genetic knockout does not target osteoclasts directly,

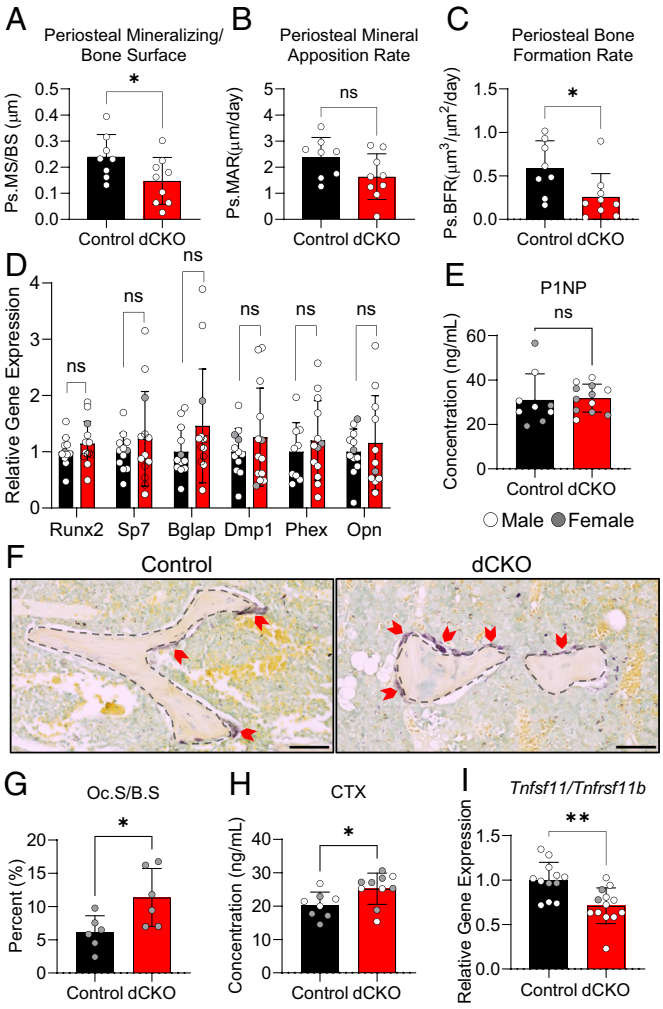

Fig. 3. Slower bone basal periosteal bone formation in Ocn-cre:*Camk2d/Camk2g* dCKO mice. Quantification of dynamic histomorphometry in the ulna of 8-wk-old male mice after IP injections of alizarin red and calcein 5 d apart (*A*) periosteal mineralizing surface/bone surface, (*B*) periosteal mineral apposition rate, and (*C*) periosteal bone formation rate (n = 8). (*D*) Relative gene expression from 3-wk-old male (white) and female (gray) marrow flushed whole-bone extracts for *Runx2*, *Sp7* (osterix), *Bglap* (osteocalcin), *Dmp1*, *Phex*, and *Opn* (control n = 12, dCKO n = 13). (*E*) Serum ELISA of amino-terminal pro-peptide of type 1 collagen (P1NP) from 8-wk-old male (white) and female (gray) mice (control n = 9, dCKO n = 12). (*F*) Representative images of tartrate-resistant acid phosphatase (TRAP) staining in the trabecular compartment of decalcified paraffin-sectioned 8-wk-old female femurs. Red arrowheads indicate TRAP positivity and black dashed lines indicate the perimeter of the trabecular bone. The scale bar represents 10 μm.) (*G*) Quantification of TRAP-positive osteoclast surface/bone surface (n = 6). (*H*) Serum ELISA of CTX from 8-wk-old male (white) and female (gray) mice (control n = 8, dCKO n = 10). (*I*) The ratio of the relative gene expression of *Tnfrsf11* (RANKL) / *Tnfrsf11b* (OPG) in 3-wk-old male (white) and female (gray) marrow flushed whole-bone extracts (control n = 12, dCKO n = 13). Graphs display the average ± SD. All data were analyzed with an unpaired *t* test except for *Bglap* and *Dmp1* RT-qPCR results, which were analyzed with a Mann–Whitney test due to nonnormal distribution.

we suspected that osteocytic and osteoblastic RANKL and OPG could be mediating the effect on osteoclasts. Osteocyte RANKL controls osteoclast formation on bone surfaces in competition with its decoy receptor, osteoblast OPG (27, 28). Accordingly, we examined the expression of RANKL (*Tnfsf11*) and OPG (*Tnfrsf11b*) and their ratios by RT-qPCR (Fig. 3*I*). Alone, neither *Tnfsf11* (*SI Appendix*, Fig. S4*K*) nor *Tnfrsf11b* (*SI Appendix*, Fig. S4*L*) gene expression is statistically changed between control and dCKO mice. However, the RANKL/OPG mRNA ratio would suggest decreased rather than increased osteoclast ratio and suggests alternative reasons for increased osteoclasts.

Skeletal Fragility in Ocn-Cre:*Camk2d/Camk2g* Double Knockout Mice. During dissection of the *Camk2d/g* dCKO mice, we noted the skeletal fragility of these mice, observing frequent iatrogenic fractures during routine dissection (Fig. 4 *A* and *B*). Accordingly, we tested the mechanical properties of femurs from *Camk2d/g* dCKO and control mice by four-point bending (Fig. 4*C*). Traces from the load cell show a distinct clustering of the control mice and *Camk2d/g* dCKO mice separately from one another (Fig. 4*D*). The separation in traces between the genotypes translated into a significantly weaker bones due to a reduction in yield load, maximum load, and failure load, with no significant difference between the ratio of maximum/failure load (Fig. 4 *E–H*). Furthermore, the *Camk2d/g* dCKO mice have less stiff bones, compared to the control mice (Fig. 4*I*), and they are also less tough than the control bones as determined by yield work and total work (Fig. 4 *J* and *K*). Yield displacement was significantly less in the *Camk2d/g* dCKO mice than the control mice, whereas postyield displacement was slightly higher although not statistically significant (Fig. 4 *L* and *M*). The *Camk2d/g* dCKO mice yield with less displacement than the control mice; therefore, they have more brittle bones. In total, the femurs of *Camk2d/g* dCKO mice exhibited significant defects in mechanical properties, as well as bone mass, which likely combine to yield skeletal fragility.

Sclerostin Abundance Is Not a Likely Driver of the *Camk2d/g* dCKO Skeletal Phenotype. Given our prior work demonstrating that CaMKII signaling is essential to the regulation of sclerostin protein abundance in response to distinct bone anabolic cues, we examined whether changes in sclerostin protein might contribute to low bone mass in this *Camk2d/g* dCKO model. Osteopenia can be caused by excess sclerostin protein abundance, which inhibits Wnt/β-catenin signaling in osteoblasts and ultimately prevents osteoblast activation and bone deposition. Since CaMKII is a required step in the degradation of sclerostin by lysosomes in osteocytes in response to mechanical load and parathyroid hormone signaling (7), we anticipated the knockout of *Camk2d/g* to result in a defect in lysosomes and an accumulation of sclerostin protein. While the ideal experiment would be to test these mice under axial loading conditions, the severe skeletal phenotype and dramatically altered mechanical properties of these bones precluded testing the role of *Camk2d/g* in the context by which the lysosomal degradation of sclerostin was shown to be relevant to load-induced bone formation (7). Instead, we examined sclerostin in mice unchallenged by exogenous axial mechanical loading. In contrast to our prediction, circulating levels of sclerostin in the sera measured with ELISA (Fig. 5*A*) and western blots of whole-bone extract from *Camk2d/g* dCKO mice revealed significantly less sclerostin protein in dCKO mice than control littermates (Fig. 5 *B* and *C*). The expression of *Sost* mRNA in whole-bone extracts was not statistically different in the *Camk2d/g* dCKO mice (Fig. 5*D*). Notably, due to the reduced bone volume in the *Camk2d/g* dCKO mice, osteocyte number was significantly reduced in *Camk2d/g* dCKO mice (Fig. 5 *E* and *F*) although osteocyte density was unchanged (Fig. 5*G*). Fewer osteocytes may explain the reduced circulating and bone-derived sclerostin abundance.

In contrast to sclerostin levels, we observed reduced LC3BII/I ratio and reduced LAMP1 protein in *Camk2d/g* dCKO mice (Fig. 5 *H–K*), suggestive of defective lysosomal activity and consistent with our hypotheses regarding CaMKII and lysosomal degradation. Nonetheless, it is unlikely that reduced, rather than increased sclerostin protein, was a driver of low bone mass in this model. If accumulated sclerostin was not a contributor to the observed osteopenia and fragility in *Camk2d/g* dCKO mice, we asked what other factors could result in low bone mass and reduced

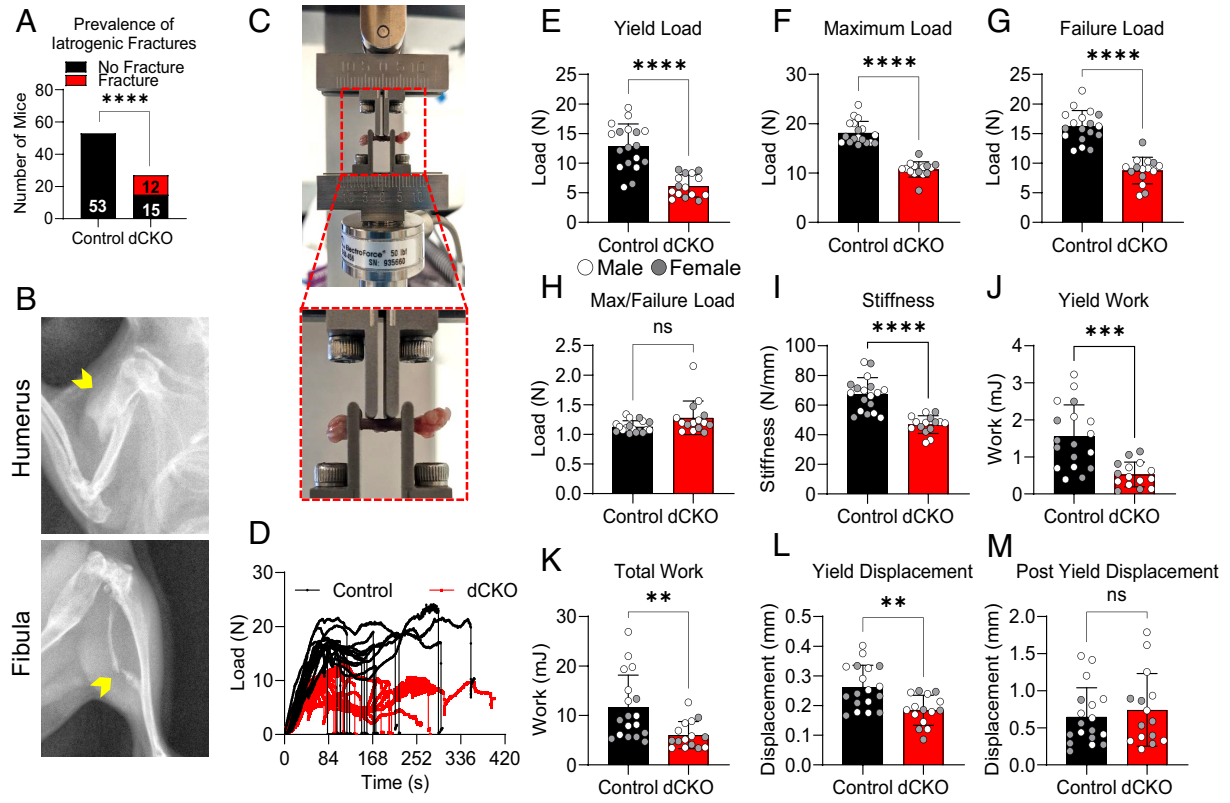

Fig. 4. Skeletal fragility in Ocn-cre:*Camk2d*/*Camk2g* dCKO mice. (*A*) Prevalence of observed iatrogenic fractures in dCKO mice (control n = 53, dCKO n = 27). (*B*) Radiographs of iatrogenic fractures, yellow arrowheads, in the humerus and fibula of dCKO mice. (*C*) A picture of an 8-wk-old femur in the four-point bending rig with an expanded view of the femur positioning in the red dashed line box. (*D*) Raw traces from four-point bending of control (black) and dCKO (red) femurs (control n = 18, dCKO n = 15). Measurements made from the raw data of male (white) and female (grey) four-point bending traces including (*E*) yield load, (*F*) maximum load, (*G*) failure load, (*H*) maximum/failure load, (*I*) stiffness, (*J*) work to yield, (*K*) total work, (*L*) yield displacement, and (*M*) postyield displacement. Graphs display the average ± SD with an unpaired *t* test analysis of the data.

mechanical properties in bone. Often fragility is associated with changes in mineral homeostasis and/or changes in fibrillar collagen. Thus, we examined these two parameters in control and *Camk2d/g* dCKO mice.

Defective Phosphate Homeostasis in *Camk2d/g* dCKO Mice with Implications of FGF23 (Fibroblast Growth Factor 23) and Alkaline Phosphatase. To assess mineral homeostasis, we examined blood chemistries from control and *Camk2d/g* dCKO mice. These dCKO mice exhibited hypophosphatemia with normal circulating calcium (Fig. 6 *A* and *B*) with no other changes in renal function save for a reduction in serum creatinine (*SI Appendix*, Fig. S5 *A–L*). Given the osteoblast/osteocyte-specific lineage deletion of *Camk2d/g,* the skeletal phenotype, and the hypophosphatemia, we examined FGF23 in these mice. FGF23 is a peptide hormone secreted by osteoblasts and osteocytes in response to high levels of circulating phosphate, where it acts to reduce circulating phosphate by preventing phosphate reuptake in the kidney and promoting excretion in the urine (29, 30). Excessive FGF23 signaling reduces serum phosphate and causes low bone mass and defective matrix mineralization, among other symptoms, in hypophosphatemic rickets/osteomalacia (30). Indeed, FGF23 protein and mRNA abundance were elevated in whole-bone extracts in the dCKO mice relative to the control mice (Fig. 6 *C–E*). Likewise, increased numbers of FGF23-positive osteocytes were observed in cortical bone sections by immunofluorescence (*SI Appendix*, Fig. S5*M*). Importantly, circulating intact FGF23 protein was also increased in the serum of dCKO mice relative to controls (Fig. 6*F*), consistent with increased abundance of bone-derived FGF23. Circulating parathyroid hormone, which can also influence FGF23 levels and phosphate status, was unchanged between control and dCKO mice (*SI Appendix*, Fig. S5*N*).

Hypophosphatemia is associated with under-mineralized bones, an outcome which could contribute to the strikingly weaker bones observed in dCKO mice (31). Accordingly, we examined the mineralization status of age-matched mice with two different outcomes. First, we implemented Otsu thresholding, a nonbiased strategy to threshold and bin voxels of μCT-scanned femurs (32). The Otsu thresholding is then calibrated to phantoms of known mineral density, establishing low (0.27 to 0.93 g/cm^3 CaHA), medium (0.94 to 1.68 g/cm^3 CaHA), and high (>1.68 g/cm^3 CaHA) density bone (Fig. 6*G*). Consistent with a hypo-mineralized bone phenotype, the fraction of cortical bone volume that was composed of low- and medium-density bone was significantly increased in the *Camk2d/g* dCKO mice relative to control mice with a proportional decrease in high-density bone (Fig. 6 *H–J*). Second, von Kossa/Van Gieson and Goldner's Trichrome histological stains of the distal femur and the vertebra revealed prominent osteoid seams in the dCKO mice consistent with hypo-mineralized bone common in hypophosphatemia (Fig. 6 *K* and *L*).

In addition to changes in bone-derived and systemic FGF23, we observed a marked reduction in TNAP (tissue non-specific alkaline phosphatase) protein in whole-bone extracts (Fig. 6 *M* and *N*), despite no change in *Tnap* transcript (Fig. 6*O*). Bone-derived alkaline phosphatase plays a critical role in bone mineralization, and global loss of TNAP or conditional deletion of TNAP in osteoblast-lineage cells in mice is associated with hypophosphatasia to varying degrees, with skeletal manifestations that include

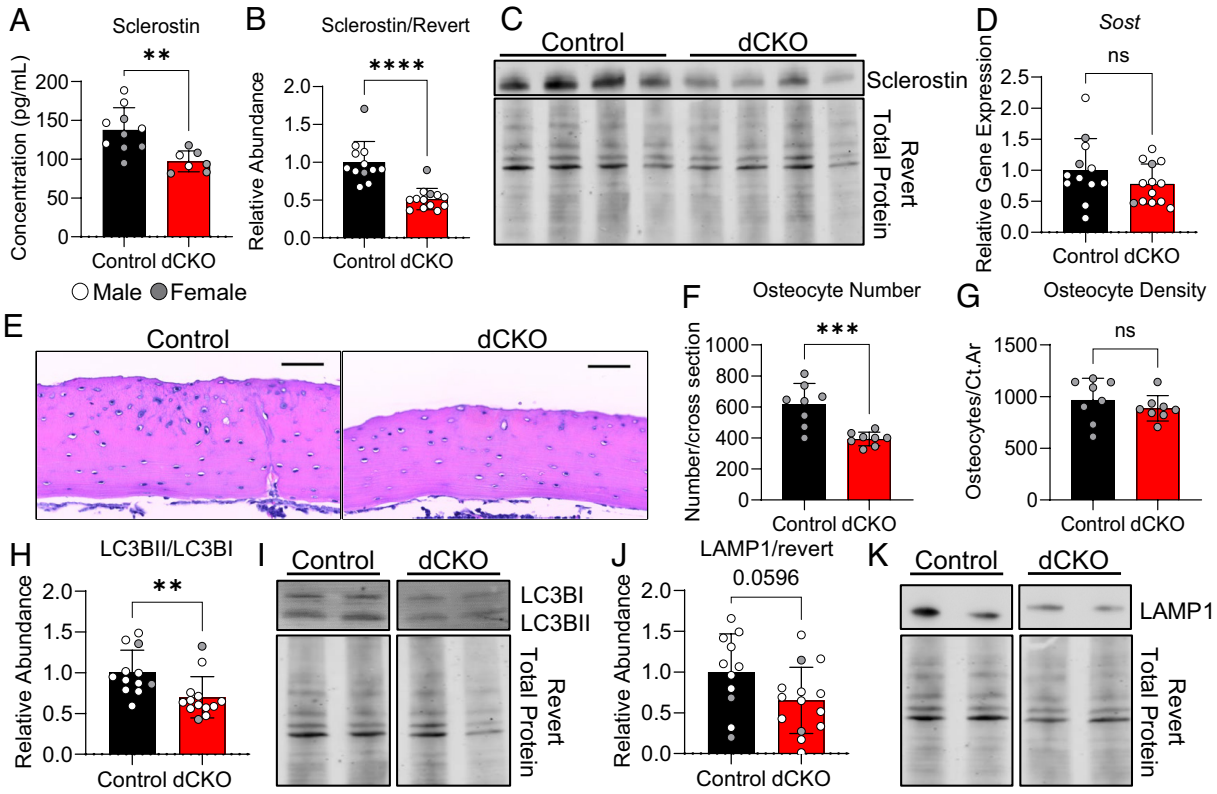

Fig. 5. Sclerostin abundance is not a likely driver of the Ocn-cre:*Camk2d*/*Camk2g* dCKO skeletal phenotype. (*A*) Serum ELISA of sclerostin from 8-wk-old male (white) and female (gray) mice (control n = 10, dCKO n = 7). (*B* and *C*) Western blot of sclerostin protein from 3-wk-old male (white) and female (gray) marrow flushed tibial extract, quantified relative to Revert total protein stain (control n = 12, dCKO n = 13). (*D*) Relative gene expression of *Sost* from 3-wk-old male (white) and female (gray) marrow flushed whole-bone extract (control n = 12, dCKO n = 13). (*E*) Representative H&E staining of decalcified paraffin-embedded femoral cross-sections from 8-wk-old female mice. The scale bar indicates 100 μm. Quantification of (*F*) osteocyte number/cross section and (*G*) osteocyte density using cortical bone area, from 8-wk-old female mice (n = 8). Western blots from 3-wk-old male (white) and female (gray) marrow flushed tibial extract for (*H* and *I*) LC3BII/I protein ratio, and (*J* and *K*) LAMP1 protein normalized to Revert total protein stain (control n = 12, dCKO n = 13). Graphs display the average ± SD with an unpaired *t* test analysis of the data.

osteopenia, fracture, and defective matrix mineralization (33–35). Importantly, while we observed decreased bone-derived TNAP, circulating alkaline phosphatase in the sera was not different between control and dCKO mice (Fig. 6*P*), suggesting that osteocalcin-directed deletion of *Camk2d*/*Camk2g* is not sufficient to cause systemic hypophosphatasia. While it is not clear the respective contributions of FGF23 and/or bone alkaline phosphatase to the phenotype of these mice, the reduction in circulating phosphate and a deficit in the ability to clear pyrophosphate locally by TNAP activity, both likely contribute to the hypomineralization phenotype observed here. Together, these data reveal an axis between CaMKIIδ/CaMKIIγ and phosphate homeostasis systemically (FGF23) and locally (TNAP) to maintain bone mass and quality.

Changes to Collagen Composition and Organization May Also Contribute to the dCKO Bone Phenotype. In addition to mineralization, changes in osteoid can also result in skeletal fragility (36, 37). Osteoid, the organic fraction of bone, is laid down by osteoblasts and is composed of proteoglycans, glycoproteins, and collagen fibers. Polarized light microscopy and Picrosirius red staining of collagen revealed a small but detectable shift in birefringence hue towards red and away from yellow/green in the *Camk2d/g* dCKO cortical bone (Fig. 7 *A* and *B*), consistent with more organized or crosslinked collagen fibers (Fig. 7*C*). RT-qPCR revealed small increases in several genes associated with collagen abundance and crosslinking, including *Col1a1*, *Lox* (lysyl oxidase), *Plod1-3,* and the collagen chaperone *Serpinh1* (Hsp47) (Fig. 7*D*). However, the magnitude of these changes appeared rather small and their contribution above those observed for altered phosphate homeostasis is not clear.

Discussion

We present an essential role for *Camk2d* and *Camk2g* in osteocalcin-cre expressing cells of the osteoblast/osteocyte lineage for the postnatal accumulation of bone mass and quality. While our initial goal was to test these mice in the context of mechanical loading, the phenotype of these mice included unexpectedly severe osteopenia and skeletal fragility spanning the axial and appendicular skeleton. We were surprised at the severity of the skeletal phenotype, which was comparable to or more severe than the osteopenia observed for the conditional deletion of some other signaling molecules with fundamental functions in bone mass acquisition (e.g., Osx-cre deletion of β-catenin, Ocn-cre deletion of p38, and Col1a1-cre deletion of Presenilin1/2 (38–40)). Few reports in the literature had mentioned any role for CaMKIIδ or CaMKIIγ in osteoblast or osteocyte biology. The few prior reports present were largely in cultured osteoblast cell lines and suggested that CaMKII may subtly regulate osteogenic differentiation by targeting various transcription factors, including Ap-1 (17), Dlx5 (41), osterix (42), or Runx2 (43). A recent study implicated CaMKII in the osteopenic phenotype of TMCO1 (an endoplasmic reticulum Ca2+ leak channel) knockout mice via its influence on Runx2 degradation (18). While we observed a severe impact on bone mass,

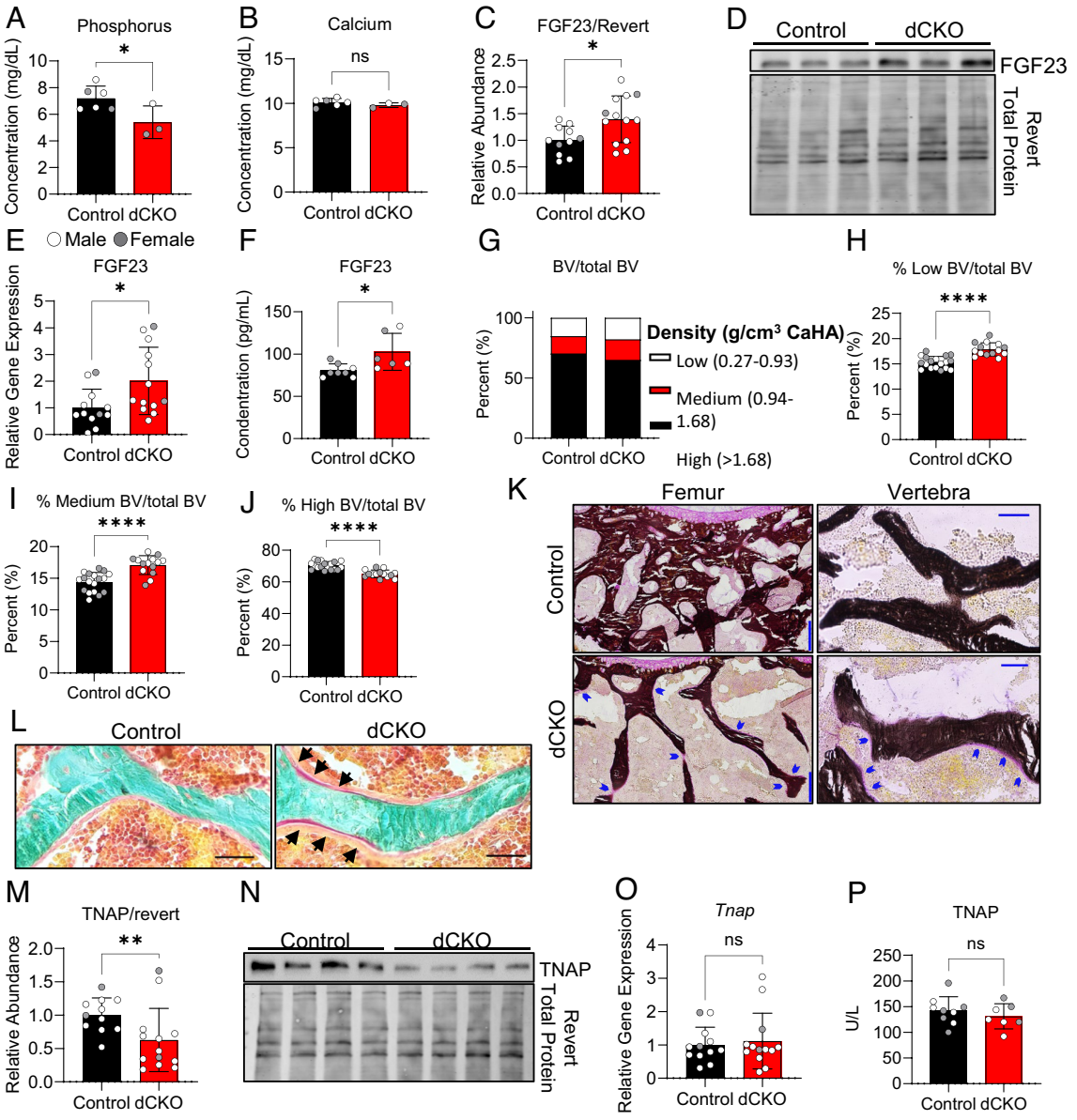

Fig. 6. Hypophosphatemia, elevated FGF23 signaling, decreased alkaline phosphatase, and hypo-mineralization are consequences of Ocn-cre:*Camk2d*/*Camk2g* dCKO. Serum chemistry from 8-wk male (white) and female (gray) mice for (*A*) phosphorus and (*B*) calcium (control n = 6, dCKO n = 3). (*C* and *D*) Western blot of FGF23 protein from 3-wk-old male (white) and female (gray) marrow flushed tibial extract, quantified relative to Revert total protein stain (control n = 11, dCKO n = 13). (*E*) Relative gene expression of *Fgf23* transcript from 3-wk-old male (white) and female (gray) marrow flushed whole-bone extract (control n = 12, dCKO n = 13). (*F*) Concentration of serum FGF23 protein from 8-wk male (white) and female (gray) mice (control n = 8, dCKO n = 6). (*G–J*) Otsu thresholding of μCT scanned 8-wk male (white) and female (gray) femurs (control n = 18, dCKO n = 14). Calibrated to 0.25 g/cm^3 and 0.75 g/cm^3 phantoms, the thresholding generated low (0.27 to 0.93 g/cm^3 CaHA), medium (0.94 to 1.68 g/cm^3 CaHA), and high (>1.68 g/cm^3 CaHA) density bone. (*G*) Bone volume of each density was compared related to total bone volume. Comparisons were made between (*H*) low-density, (*I*) medium-density, and (*J*) high-density bone in the Control and dCKO mice. (*K*) Representative von Kossa/Van Gieson staining of nondecalcified MMA embedded femoral and vertebral sections with blue arrowheads indicating osteoid seam. The scale bar represents 100 μm in the femur and 50 μm in the vertebra. (*L*) Goldner's trichrome staining with black arrows indicating unmineralized osteoid seam (magenta) on the trabecular bone surface (green) in MMA sectioned vertebra. The scale bar indicates 50 μm. (*M* and *N*) Western blot of TNAP protein from 3-wk-old male (white) and female (gray) marrow flushed tibial extract, normalized to Revert total protein stain (control n = 11, dCKO n = 13). (*O*) Relative gene expression of *Tnap* from 3-wk-old male (white) and female (gray) marrow flushed whole-bone extract (control n = 12, dCKO n = 13). (*P*) Concentration of serum TNAP from 8-wk-old male (white) and female (gray) control (n = 9) and dCKO (n = 7) mice. Graphs display the average ± SD. After testing normalization, normal data were analyzed with an unpaired *t* test whereas nonnormal data were analyzed with a Mann–Whitney test.

in contrast to these studies, we did not observe a widespread, cell-autonomous effect of CaMKII deletion on osteoblast differentiation in vivo or in vitro. In vitro and in vivo osteoblast gene expression was largely and surprisingly unaffected by *Camk2d*/*g* deletion, and in vivo impacts on osteoblast function were envelope specific, occurring in the periosteum and trabecular compartment, but not the endosteum. However, one consistent finding between our study and most of these prior in vitro studies was the decrease in osteoblast-lineage alkaline phosphatase with loss of CaMKII function (17, 18, 41, 42). Although this reduction in bone-derived TNAP was not sufficient to induce systemic hypophosphatasia.

Despite in vitro studies suggesting a potential impact of CaMKII signaling on alkaline phosphatase, we were surprised to find that this mouse model had hypophosphatemia. Neither regulation of FGF23 nor circulating phosphate by CaMKII has been previously described. Indeed *Camk2d*/*Camk2g* double knockout mice share some, but not all, of the skeletal phenotypes of the Hyp mouse, the mouse model of overexpression of FGF23, and

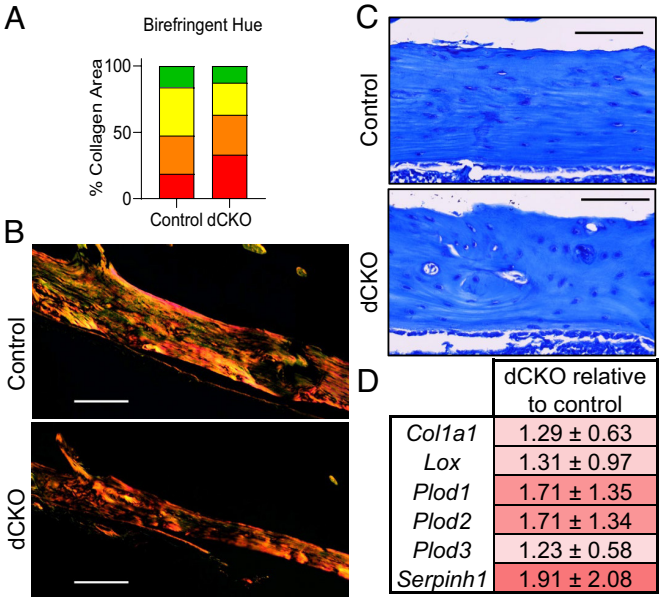

	dCKO relative to control
Col1a1	1.29 ± 0.63
Lox	1.31 ± 0.97
Plod1	1.71 ± 1.35
Plod2	1.71 ± 1.34
Plod3	1.23 ± 0.58
Serpinh1	1.91 ± 2.08

Fig. 7. Changes to collagen composition and organization contribute to the Ocn-cre:*Camk2d*/*Camk2g* dCKO phenotype. (*A* and *B*) Quantification and representative images of pircro sirius red staining of 8-wk-old decalcified paraffin embedded longitudinal femur sections (n = 6). Birefringent hue was broken into four bins; red, orange, yellow, and green. The scale bar represents 100 μm. (*C*) Toluidine blue staining of 8-wk-old decalcified paraffin-embedded longitudinal femur sections. The scale bar represents 100 μm. (*D*) Relative gene expression from 3-wk-old mice of various collagen/collagen processing/collagen cross-linking transcripts including, *Col1a1*, *Lox*, *Plod1*, *Plod2*, *Plod3*, and *Hsp47* (control n = 12, dCKO n = 13). Data are presented as the mean ± SD.

the systemic or osteoblastic-conditional deletion of TNAP (34, 35, 44, 45). Like these models, we observed many of the tell-tale signs of phosphate homeostasis dysfunction, including hypo-mineralized bone, a significant increase in the osteoid seam, and decreased trabecular and cortical bone mass, but we did not see a reduction in body weight or limb length. Notably, a prior study observed that injection of CaMKII inhibitor into calvaria of mice for 7 d resulted in hypomineralized bone, which, while not explicitly reported, appeared to contain unmineralized or undermineralized osteoid seams that closely parallels our observations (17). We observed decreases in both serum phosphate and bone-derived alkaline phosphatase, which both could influence bone mineralization. However, it is important to note that circulating alkaline phosphatase was unaffected, perhaps due to compensation from other sources. Whether the mineralization phenotype is explained by elevated FGF23 (hypophosphatemia), decreased TNAP-dependent hydroxyapatite nucleation, or both is not clear. Nonetheless, the overlap of skeletal phenotype between our model and other models of hypophosphatemia and local deletion of TNAP in bone is consistent with *Camk2d*/*Camk2g* in bone playing a major role in phosphate homeostasis.

In addition to the regulation of phosphate homeostasis, we did uncover some other roles for CaMKII in late osteoblasts and osteocytes, which may also contribute to the phenotype. As mentioned above and in contrast to the in vitro literature on the role of CaMKII on osteoblast differentiation, a clear cell-autonomous defect in osteoblast differentiation was not detected in vitro or in vivo. Rather, osteoblast activity, and perhaps to a lesser extent osteoblast number, was disrupted on periosteal and trabecular but not endocortical bone surfaces. While others had seen a cell-autonomous effect on the osteoblast lineage, this may be due to the fact that these other studies did not specifically target *Camk2d* or *Camk2g* and often relied on pharmacological inhibition or siRNA-mediated targeting of other CaMKII genes, such as *Camk2a* (17, 42, 43). We also detected increased osteoclast surface/trabecular bone surface, although this change was not predicted by the ratio of RANKL and OPG gene expression. Since we observed changes in both bone formation and resorption, we propose that there is a secreted factor modifying both osteoblasts and osteoclasts as a consequence of CaMKIIδ/γ in osteoblast lineage cells.

Our hypothesis predicted that sclerostin may be the secreted factor modified by conditional codeletion of CaMKIIδ/CaMKIIγ responsible for the severity of low bone mass in these mice, because we had previously performed experiments showing activation of CaMKII in response to mechanical load is necessary to degrade sclerostin protein (6, 7, 19). However, whether the requirement of CaMKIIδ and CaMKIIγ to degrade sclerostin extrapolates to a control of bone formation in vivo had not yet been confirmed. Initially, we had planned to test in vivo mechano-responsiveness using sclerostin as an output in the dCKO mice using an axial bone load model; however, the severe differences in mechanical properties of these bones precluded us from doing these experiments. Instead, we evaluated sclerostin protein and gene expression in mice in the basal state unchallenged by exogenous axial loading. In contrast to what we had predicted, sclerostin protein abundance was decreased rather than increased in the bones or serum of *Camk2d/g* dCKO at least in the absence of loading challenge. While there are reports that demonstrate a regulatory relationship between sclerostin and FGF23 protein, our observations do not appear to exhibit this dynamic as we have low sclerostin abundance and high FGF23 abundance (46, 47). Thus, it is likely that the effects on sclerostin and FGF23 are common to CaMKII activity rather than a direct effect of sclerostin on FGF23. Interestingly, it appeared that lysosome activity was disrupted as we had hypothesized. We have several possible reasons why sclerostin was unexpectedly reduced rather than elevated in this model. In the absence of loading in vitro, we found that sclerostin protein half-life is on an hour's timescale and its route of degradation (proteasome or lysosome) is different than in the context of loading (7, 8). Only with applied mechanical loading in vivo or in vitro did we observe the rapid, minutes timescale degradation of sclerostin via the lysosome (7, 8). Another possibility is that *Camk2d/g* dCKO mice had less bone and less osteocytes than control mice. Since sclerostin is produced by osteocytes, a reduction in osteocyte number may result in a net decrease in sclerostin. Additionally, the bones of these dCKO mice may experience more mechanical strain from normal cage activity than control bones given their osteopenia and mechanical property defects. This could act as a greater mechanical stimulus in dCKO mice than in controls, ultimately leading to a reduction in sclerostin protein at the ages we examined. Finally, chronic loss of CaMKII may have distinct effects from its transient inhibition or activation by acute bone anabolic signals, and these effects may influence the sclerostin encoding gene, *Sost*. We observed a slight but not statistically significant decrease in *Sost* mRNA in *Camk2d/g* dCKO mice. Pharmacologic inhibition of CaMKII has been shown to decrease *Sost* mRNA in vitro in OCY454 osteocyte-like cells (48). Likewise, CaMKII has been shown to regulate HDAC4/MEF2c signaling in cardiac muscle (49). In osteocytes, HDAC4/5 regulates MEF2c binding to the upstream ECR5 enhancer region controlling *Sost* gene expression (50, 51). Therefore, it is possible that we see a decrease in sclerostin protein and a modest decrease in *Sost* transcript not only from fewer osteocytes or an altered strain environment but also perhaps due to transcriptional repression. Future work will examine the role of mechanical loading in these *Camk2d/g* dCKO using an inducible Cre model that allows us to

circumvent some of the more profound effects on mechanical properties, bone mass, and osteocyte numbers.

Interestingly, the change in TNAP protein, but not gene expression, as well as the change in osteoclast number and activity despite an opposing RANKL/OPG gene expression ratio that we observed in this study suggests that one role for CaMKII may be in the posttranslational control of proteins in osteoblasts and osteocytes. Likewise, our previously reported regulation of sclerostin protein abundance downstream of CaMKII involved posttranslational control. Notably, CaMKII plays an important role in protein trafficking and secretion in neuronal cells and pancreatic beta-cells (52) and may serve a similar, largely unexplored role in bone.

Finally, we observed changes in some genes associated with collagen production, as well as changed in collagen crosslinking and maturation. However, these changes were relatively subtle. Further, we did not observe substantial changes in the postyield properties of these bones, suggesting that this may only be a negligible contributor to the observed bone phenotype.

In conclusion, we demonstrated a previously unknown and profound role of *Camk2d* and *Camk2g* in cells of the osteoblast lineage. These mice exhibit severe osteopenia and compromised mechanical properties, as a result of compartment-specific decreased osteoblast activity, increased osteoclasts number and activity, and disrupted phosphate homeostasis consistent with hypophosphatemia and reduced bone-derived alkaline phosphatase. While our prior work revealed that CaMKII may be an integrator of mechanical loading and other bone anabolic cues in the control of sclerostin, we now reveal CaMKII in bone as an essential signaling node underscoring pathways involved with phosphate homeostasis, maintenance of bone mass, and matrix mineralization.

Materials and Methods

Animals. Floxed *Camk2d/g* mice were generously provided by the Olson group (23) and were crossed into osteocalcin-cre (OC-cre) mice (RRID:IMSR_JAX:019509) (24), to generate late osteoblast/osteocyte specific deletion of *Camk2d/g*. For most breeding pairs, a cre- dam/cre+ sire breeding strategy was used. Cre-positive mice containing two conditionally knocked out *Camk2d/g* alleles are the experimental dCKO mice, while homozygous fl/fl littermates without the cre allele served as controls. Genotyping primers and expected band size are listed below in *SI Appendix*, Table S1. At 8 wk of age, control n = 19 (10 male, 9 female) and dCKO n = 17 (10 male, 7 female) mice were collected. At 3 wk of age, control n = 13 (10 male, 3 female) and dCKO n = 16 (11 male, 5 female) mice were collected. Photos were taken postsac next to a ruler to measure the length of the mouse from snout to butt (tails were excluded due to tail snip collection for genotyping). Eight-week-old mice were X-rayed in the anterior-posterior and lateral views using a Faxitron digital X-ray system as described (53). Additional 8-wk mice were analyzed using DXA, control n = 12 (5 male, 7 female), and dCKO n = 4 (2 male, 2 female). A separate group of 8-wk mice were used for serum chemistry control n = 6 (4 male, 2 female) and dCKO n = 3 (1 male, 2 female). The last group of 8-wk mice control n = 9 (4 male, 5 female) and dCKO n = 7 (4 male, 3 female) provided skulls for μCT analysis of occipital/supra-occipital bone volume, and serum for FGF23 ELISA and serum TNAP. Another cohort of 8-wk male mice, control n = 4, dCKO n = 4, had serum collected for PTH ELISA. Finally, P1 mice (n = 5) were processed for whole-mount staining (control n = 3, dCKO n = 2). All animal procedures were approved by the University of Maryland School of Medicine's Institutional Animal Care and Use Committee and mice were group housed with ad libitum access to food/water.

Statistics. Normality of the data was analyzed using GraphPad Prism and was used to subsequently analyze significance with either an unpaired *t* test (normally distributed) or Mann–Whitney test (nonnormally distributed). Data are graphed as the average ± SD. Asterisks represent the following *P* values: $*P < 0.05$, $**P < 0.01$, $***P < 0.001$, $****P < 0.0001$. Male and female data were analyzed separately and there was no evidence that sexual dimorphism was contributing to this phenotype. Therefore, data we present combine both sexes together with an indication of which datapoints are male (white) and female (gray).

Data, Materials, and Software Availability. All study data are included in the article and/or *SI Appendix*.

ACKNOWLEDGMENTS. We acknowledge Dr. Eric Olson for providing the *Camk2d*$^{fl/fl}$/*Camk2g*$^{fl/fl}$ mice (Molecular Biology, University of Texas Southwestern). We also acknowledge Dr. Sergey Leikin for teaching the four point bending procedure and analysis as well as his suggestions regarding this project (Physical Biochemistry, NIH). For paraffin-embedded long bong histology sections, we acknowledge the University of Maryland School of Medicine's & Greenebaum Comprehensive Cancer Center's Pathology Biorepository Shared Services–Baltimore, Maryland. This publication was supported by funds through the Maryland Department of Health's Cigarette Restitution Fund Program and the National Cancer Institute–Cancer Center Support Grant–P30CA134274. We thank Jean Garcia-Diaz and Dr. Ryan C. Riddle for teaching MMA (methyl-methacrylate) embedding and bone sectioning (Department of Orthopaedics, University of Maryland School of Medicine). We also thank Dr. Suzanne Jan de Beur for her expertise and comments regarding the interpretation of our data (Department of Endocrinology, The Johns Hopkins University School of Medicine). Our research is supported by the NIH, National Institute of Arthritis and Musculoskeletal and Skin Diseases research grant R01-AR071614-05.

1. N. R. Gould, O. M. Torre, J. M. Leser, J. P. Stains, The cytoskeleton and connected elements in bone cell mechano-transduction. *Bone* **149**, 115971 (2021), 10.1016/j.bone.2021.115971.
2. J. Delgado-Calle, T. Bellido, The osteocyte as a signaling cell. *Physiol. Rev.* **102**, 379–410 (2022).
3. L. F. Bonewald, The amazing osteocyte. *J. Bone Miner. Res.* **26**, 229 (2011).
4. T. Komori, Functions of the osteocyte network in the regulation of bone mass. *Cell Tissue Res.* **352**, 191–198 (2013).
5. C. Palumbo, M. Ferretti, The osteocyte: From 'prisoner' to 'orchestrator'. *J. Funct. Morphol. Kinesiol.* **6**, 28 (2021).
6. J. S. Lyons *et al.*, Microtubules tune mechanotransduction through NOX2 and TRPV4 to decrease sclerostin abundance in osteocytes. *Sci. Signal.* **10**, eaan5748 (2017).
7. N. R. Gould *et al.*, Disparate bone anabolic cues activate bone formation by regulating the rapid lysosomal degradation of sclerostin protein. *Elife* **10**, e64393 (2021).
8. K. M. Williams *et al.*, TRPV4 calcium influx controls sclerostin protein loss independent of purinergic calcium oscillations. *Bone* **136**, 115356 (2020).
9. S. Tanaka, T. Matsumoto, Sclerostin: From bench to bedside. *J. Bone Miner. Metab.* **39**, 332–340 (2020).
10. T. Tobimatsu, H. Fujisawa, Tissue-specific expression of four types of rat calmodulin-dependent protein kinase II mRNAs. *J. Biol. Chem.* **264**, 17907–17912 (1989).
11. R. Yasuda, Y. Hayashi, J. W. Hell, CaMKII: A central molecular organizer of synaptic plasticity, learning and memory. *Nat. Rev. Neurosci.* **23**, 666–682 (2022).
12. O. E. R. Gaido *et al.*, CaMKII as a therapeutic target in cardiovascular disease. *Annu. Rev. Pharmacol. Toxicol.* **63**, 249–272 (2023), 10.1146/annurev-pharmtox-051421-111814.
13. S. Ally, A. L. Jolly, V. I. Gelfand, Motor-cargo release: CaMKII as a traffic cop. *Nat. Cell Biol.* **10**, 3–5 (2008).
14. X. Li *et al.*, CaMKII-mediated Beclin 1 phosphorylation regulates autophagy that promotes degradation of Id and neuroblastoma cell differentiation. *Nat. Commun.* **8**, 1159 (2017).
15. F. A. Vigil, K. P. Giese, Calcium/calmodulin-dependent kinase II and memory destabilization: A new role in memory maintenance. *J. Neurochem.* **147**, 12–23 (2018).
16. C. T. Bussey, J. R. Erickson, Physiology and pathology of cardiac CaMKII. *Curr. Opin. Physiol.* **1**, 52–58 (2018).
17. M. Zayzafoon, K. Fulzele, J. M. McDonald, Calmodulin and calmodulin-dependent kinase IIalpha regulate osteoblast differentiation by controlling c-fos expression. *J. Biol. Chem.* **280**, 7049–7059 (2005).
18. J. Li *et al.*, TMCO1-mediated Ca2+ leak underlies osteoblast functions via CaMKII signaling. *Nat. Commun.* **10**, 1589 (2019).
19. N. Gould *et al.*, In vitro fluid shear stress induced sclerostin degradation and CaMKII activation in osteocytes. *Bio. Protoc* **11**, e4251 (2021).
20. M. Sumi *et al.*, The newly synthesized selective Ca2+calmodulin dependent protein kinase II inhibitor KN-93 reduces dopamine contents in PC12h cells. *Biochem. Biophys. Res. Commun.* **181**, 968–975 (1991).
21. M. N. Waxham, J. Aronowski, S. A. Westgate, P. T. Kelly, Mutagenesis of Thr-286 in monomeric Ca2+/calmodulin-dependent protein kinase II eliminates Ca2+/calmodulin-independent activity. *Proc. Natl. Acad. Sci. U.S.A.* **87**, 1273 (1990).
22. J. Spatz *et al.*, The Wnt inhibitor sclerostin is up-regulated by mechanical unloading in osteocytes in vitro. *J. Biol. Chem.* **290**, 16744–16758 (2015).
23. M. M. Kreusser *et al.*, Cardiac CaM kinase II genes δ and γ contribute to adverse remodeling but redundantly inhibit calcineurin-induced myocardial hypertrophy. *Circulation* **130**, 1262–1273 (2014).

24. M. Zhang *et al.*, Osteoblast-specific knockout of the insulin-like growth factor (IGF) receptor gene reveals an essential role of IGF signaling in bone matrix mineralization. *J. Biol. Chem.* **277**, 44005–44012 (2002).
25. S. Li *et al.*, A conditional knockout mouse model reveals a critical role of PKD1 in osteoblast differentiation and bone development. *Sci. Rep.* **7**, 1–13 (2017).
26. M. N. Knight *et al.*, R-spondin-2 is a Wnt agonist that regulates osteoblast activity and bone mass. *Bone Res.* **6**, 1–14 (2018).
27. J. Xiong *et al.*, Matrix-embedded cells control osteoclast formation. *Nat. Med.* **17**, 1235 (2011).
28. K. M. Cawley *et al.*, Local production of osteoprotegerin by osteoblasts suppresses bone resorption. *Cell Rep.* **32**, 108052 (2020).
29. S. S. Beck-Nielsen *et al.*, FGF23 and its role in X-linked hypophosphatemia-related morbidity. *Orphanet J. Rare Dis.* **14**, 58 (2019).
30. T. Shimada *et al.*, Targeted ablation of Fgf23 demonstrates an essential physiological role of FGF23 in phosphate and vitamin D metabolism. *J. Clin. Inves.* **113**, 561 (2004).
31. N. P. Camacho, C. M. Rimnac, R. A. Meyer, S. Doty, A. L. Boskey, Effect of abnormal mineralization on the mechanical behavior of x-linked hypophosphatemic mice femora. *Bone* **17**, 271–278 (1995).
32. E. C. Walker, N. E. McGregor, A. S. M. Chan, N. A. Sims, Measuring bone volume at multiple densities by micro-computed tomography. *Bio. Protoc.* **11**, e3873 (2021).
33. S. Narisawa, N. Fröhlander, J. L. Millán, Inactivation of two mouse alkaline phosphatase genes and establishment of a model of infantile hypophosphatasia. *Dev. Dyn.* **208**, 432–446 (1997).
34. K. N. Fedde *et al.*, Alkaline phosphatase knock-out mice recapitulate the metabolic and skeletal defects of infantile hypophosphatasia. *J. Bone Miner. Res.* **14**, 2015 (1999).
35. B. L. Foster *et al.*, Conditional Alpl ablation phenocopies dental defects of hypophosphatasia. *J. Dent. Res.* **96**, 81 (2017).
36. K. J. Jepsen, M. J. Silva, D. Vashishth, X. E. Guo, M. C. H. van der Meulen, Establishing biomechanical mechanisms in mouse models: Practical guidelines for systematically evaluating phenotypic changes in the diaphyses of long bones. *J. Bone Miner. Res.* **30**, 951–966 (2015).
37. M. J. Silva *et al.*, Decreased collagen organization and content are associated with reduced strength of demineralized and intact bone in the SAMP6 mouse. *J. Bone Miner. Res.* **21**, 78–88 (2006).
38. J. Chen, F. Long, β-catenin promotes bone formation and suppresses bone resorption in postnatal growing mice. *J. Bone Miner. Res.* **28**, 1160 (2013).
39. C. Thouverey, J. Caverzasio, The p38a MAPK positively regulates osteoblast function and postnatal bone acquisition. *Cell. Mol. Life Sci.* **69**, 3115–3125 (2012).
40. F. Engin *et al.*, Dimorphic effects of notch signaling in bone homeostasis. *Nat. Med.* **14**, 299 (2008).
41. J. H. Seo *et al.*, Calmodulin-dependent kinase II regulates Dlx5 during osteoblast differentiation. *Biochem. Biophys. Res. Commun.* **384**, 100–104 (2009).
42. Y. H. Choi, J. H. Choi, J. W. Oh, K. Y. Lee, Calmodulin-dependent kinase II regulates osteoblast differentiation through regulation of Osterix. *Biochem. Biophys. Res. Commun.* **432**, 248–255 (2013).
43. L. Yu *et al.*, Fluid shear stress induces osteoblast differentiation and arrests the cell cycle at the G0 phase via the ERK1/2 pathway. *Mol. Med. Rep.* **16**, 8699 (2017).
44. E. M. Eicher, J. L. Southard, C. R. Scriver, F. H. Glorieux, Hypophosphatemia: Mouse model for human familial hypophosphatemic (vitamin D-resistant) rickets. *Proc. Natl. Acad. Sci. U.S.A.* **73**, 4667 (1976).
45. X. Bai, D. Miao, J. Li, D. Goltzman, A. C. Karaplis, Transgenic mice overexpressing human fibroblast growth factor 23 (R176Q) delineate a putative role for parathyroid hormone in renal phosphate wasting disorders. *Endocrinology* **145**, 5269–5279 (2004).
46. K. A. Carpenter, R. D. Ross, Sclerostin antibody treatment increases bone mass and normalizes circulating phosphate levels in growing Hyp mice. *J. Bone Miner. Res.* **35**, 596 (2020).
47. N. Ito *et al.*, Sclerostin directly stimulates osteocyte synthesis of fibroblast growth factor-23. *Calcif. Tissue Int.* **109**, 66–76 (2021).
48. K. Ikezaki-Amada *et al.*, Extracellular acidification augments sclerostin and osteoprotegerin production by Ocy454 mouse osteocytes. *Biochem. Biophys. Res. Commun.* **597**, 44–51 (2022).
49. J. Backs *et al.*, The delta isoform of CaM kinase II is required for pathological cardiac hypertrophy and remodeling after pressure overload. *Proc. Natl. Acad. Sci. U.S.A.* **106**, 2342–2347 (2009).
50. M. N. Wein *et al.*, HDAC5 controls MEF2C-driven sclerostin expression in osteocytes. *J. Bone Miner. Res.* **30**, 400–411 (2015).
51. M. N. Wein *et al.*, SIKs control osteocyte responses to parathyroid hormone. *Nat. Commun.* **7**, 13176 (2016).
52. J. A. P. Rostas, K. A. Skelding, Calcium/calmodulin-stimulated protein kinase II (CaMKII): Different functional outcomes from activation, depending on the cellular microenvironment. *Cells* **12**, 401 (2023).
53. A. M. Buo, R. E. Tomlinson, E. R. Eidelman, M. Chason, J. P. Stains, Connexin43 and Runx2 interact to affect cortical bone geometry, skeletal development, and osteoblast and osteoclast function. *J. Bone Miner. Res.* **32**, 1727–1738 (2017).